IOP Conf. Series: Materials Science and Engineering **444** (2018) 022003 doi:10.1088/1757-899X/444/2/022003

Influence of roughness and wear on pressure distribution and stress state at wheel - rail contact

C I Bărbînţă[1] and S Creţu[2]

[1]WBN Waggonbau Niesky Gmbh, Germany
[2]Mechanical Engineering, Mechatronics and Robotics Department, "Gheorghe Asachi" Technical University of Iasi, Iasi, Romania

E-mail: costelbarbinta@yahoo.com

Abstract. The rail and wheel surfaces with numerically generated roughness have been incorporated into a computerized analysis model for concentrated contacts. In normal running operations the contacting surfaces undergo very complex loading regimes characterized by: the lack of lubrication, existence of normal, tangential and traction loads with the presence of different degrees of slippage. An inevitable wear evolves that determines time dependencies for profiles of active surfaces The role played by the running in process as well as the main roughness parameters on the pressures distribution, contact area and depth distribution of von Mises equivalent stress, have been pointed out. Important criteria as the traffic safety and maintenance costs require optimized profiles. To fulfill this requirement the knowledge of wear evolution becomes a priority and consequently the contact areas and pressures distributions corresponing to different stages of wear is one of the primary needs. The profiles measurements of new and worn wheels revield the modification in pressures distribuion, contact areas and vonMises stresses caused by time evolutuon of wear.

1. Introduction

In the field of railway transport, the current issues related to wheel-rail contact are: safety, economic, and environmental. During operation, the wheel-rail contact surface is subjected to abrasion wear and contact fatigue. At the wheel-rail interface, the evolution of abrasion wear and contact fatigue phenomena are determined by specific factors as:
- quality of the materials used to manufacture each of the two bodies representing the rolling contact ;
- location, shape and size of the contact area, pressures distribution on the contact area, and stress state created by the complex rolling contact loading with slipping;
- the presence of the third body.

The problem was first solved by Carter considering the wheel-rail contact as a cylinder rolling over a plane (a two-dimensional problem)[1, 2]. Three decades later, de Pater and Johnson [2], have predicted the shape and the size of the contact area and pressure distribution considering the Hertzian three-dimensional solution. In fact, the wheel-rail concentrated contact appears as a non-Hertzian contact because of the following violations of the Hertzian assumptions:
- the surfaces separation around the initial contact point can not be expressed as a quadratic form;
- the common generatrix has a finite length;
- the contacting surfaces are no longer smooth;
- the friction is present on the contacted area.

Apart from the approximated solutions, the general case for modelling the wheel-rail contact must be numerically solved. Kalker was the first to solve the general wheel - rail contact, for which purpose

he developed the program CONTACT [3]. For vehicle dynamics problems, where the external contact parameters change continuously, i.e. lateral position between wheel and rail profiles, the program CONTACT cannot be used due to the high computational time. To overcome this, Kalker proposed a new contact model called FASTSIM.

A survey of these methods is done in [2, 3]. Finite element methods are also applied to the wheel-rail contact problem and significant simulations and developments have been reported in literature [4].

The state-of-the-art papers from ref. [5] discuss in more detail the above methods of contact mechanics applicable for wheel - rail contact. More recent different semi-analytical algotritms were developed [6- 9] who solved the contact between two randomly shaped bodies described as half spaces by using the Papkovici - Boussinesq solution.The numerical algorithm developed by authors [6, 7] and its solving code uses the Conjugate Gradient Method involving the Discrete Convolution associated with a 3D fast Fourier transformation to obtain the displacement as a convolution of pressures with elastic influence coefficients.

In the wheel-rail contact the separation between the contacting surfaces depends on a lot of variables as: wheel profile, rail profiles, rail inclination, track gauge, inside gauge and lateral shift of the axle.

Every elastic model for contact analysis of rough surfaces presents very large local asperity contact stresses, able to exceed the yielding limit. In the case of wheel-rail contact the freshely ground surface roughness, figure1a, consists of martensitic peaks which in the first train-passes are wiped out and become part of the interfacial layer, figure1b.

Researches on rough contact using elastic or elastoplastic modeling were performed in ref. [8-17]. Also, some results on wheel-rail rough contact was obtained in [18, 19].

After the running operation, due to wear, both wheel and rail profiles undergo changes and for reasons of trafic safety, reducing maintenance costs and, last but not least of profiles optimazation the contact area and pressures distribution, figure 2 are needed to be known.

Simulation of wheel and rail profiles wear was done in [20, 21] and a comparative study between the experimental results and the mathematical modeling of wear at the wheel-rail interface was done in [22].

(a) New wheel – new rail (b)Worn wheel – worn rail

Figure 1. Different stages of the wheel and rail topography

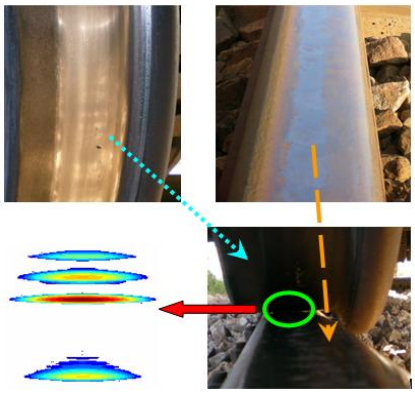

Figure 2. Wear at the wheel-rail interface

2. Determination of pressure distribution and stress state at wheel - rail contact

2.1. Analytical and numerical formulations

A hypothetical rectangular contact area denoted A_h is built on the common tangent plane, around the initial contact point. The hypothetical area is large enough to overestimate the unknown real contact area, $A_h \geq A_r$, figure 3.

A Cartesian system *(x, y, z)* is introduced, its *x-O-y* plane being the common tangent plane and with its origin located at the left corner of the hypothetical rectangular area. The sum of the individual deflections at any generic point *(x, y)* is defined as a composite deflection, denoted by *w(x, y)*.

A uniformly spaced rectangular array is built on the hypothetical rectangular contact area with the grid sides parallel to the *x* and *y*-axes, figure 3. The nodes of the grid are denoted by *(i, j)*, where indices *i* and *j* refer to the grid columns and rows, respectively.

The real pressure distribution is approximated by a virtual pressure distribution, a piecewice-constant approximation between grid nodes being typically used, figure 4.

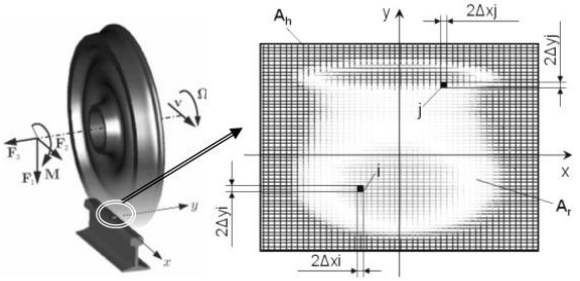

Figure 3. The real and hypothetical contact areas.

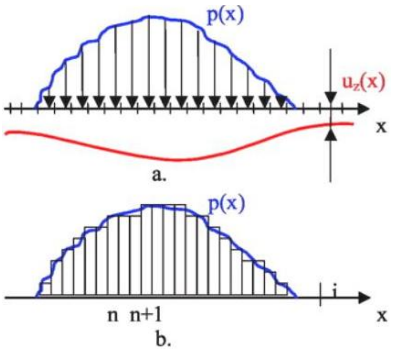

Figure 4. The real pressure distribution and piecewice-constant approximation

The model of surface deformation is defined by the following three equations:

a) the geometric equation of the elastic contact:

$$g(x,y) = h(x,y) + w(x,y) - \delta_0 \tag{1}$$

b) the integral equation of the normal surface displacement, (Boussinesq formula):

$$w(x,y) = \frac{1}{\pi}\left(\frac{1-\upsilon_I^2}{E_I} + \frac{1-\upsilon_{II}^2}{E_{II}}\right)\iint_{A_r} \frac{p(\xi,\eta)}{\sqrt{(x-\xi)^2+(y-\eta)^2}} d\xi d\eta \tag{2}$$

where: E_I, E_{II}, υ_I, υ_{II}, are Young's modulus and Poisson's ratio for the elastic materials, and $p(x, y)$ is the interfacial contact pressure;

c) the load balance equation:

$$\int_{A_r} p(x,y)dxdy = Q \tag{3}$$

where Q is the applied normal force.

The constraint equations of non-adhesion and non-penetration must be fulfilled:

$$g(x,y) = 0,\ p(x,y) > 0, (x,y) \in A_r \tag{4}$$

$$g(x,y) > 0,\ p(x,y) = 0, (x,y) \notin A_r \tag{5}$$

A uniformly spaced rectangular array is built on the hypothetical rectangular contact area with the grid sides parallel to the *x* and *y*-axes, figure 3. The nodes of the grid are denoted by *(i, j)*, where indices *i* and *j* refer to the grid columns and rows, respectively. In the considered Cartesian system, the coordinates of the grid node *(i, j)* are denoted by (x_i, y_j) and are given by $x_i = i * \Delta x$, $(0 \le i < Nx)$ and $y_j = j * \Delta y$, $(0 \le j < Ny)$ where Δx and Δy are the grid spaces in the *x* and *y*-directions, respectively. The real pressure distribution is approximated by a virtual pressure distribution, a

piecewice-constant approximation between grid nodes being typically used. The analytic formulation, represented by equations (1) - (5) is replaced by the discrete approach, equations (6) - (10):

$$g_{ij} = h_{ij} - R_{ij} + w_{ij} - \delta_0 \tag{6}$$

$$w_{ij} = \sum_{k=0}^{Nx-1} \sum_{l=0}^{Ny-1} K_{i-k,j-l} p_{kl} \tag{7}$$

$$\Delta x \Delta y \sum_{i=0}^{Nx-1} \sum_{j=0}^{Ny-1} p_{ij} = F \tag{8}$$

$$g_{ij} = 0,\ p_{ij} > 0,\ (i,j) \in A_r \tag{9}$$

$$g_{ij} > 0,\ p_{ij} = 0,\ (i,j) \notin A_r \tag{10}$$

The influence function K_{ij} describes the deformation of the meshed surface due to a unit pressure acting in element *(k, l):*

$$K_{ij} = \frac{1}{\pi}\left(\frac{1-\upsilon_I^2}{E_I} + \frac{1-\upsilon_{II}^2}{E_{II}}\right) \int_{y1}^{y2} \int_{x1}^{x2} \frac{1}{\sqrt{(x_i - \xi)^2 + (y_j - \eta)^2}} d\xi d\eta, \tag{11}$$

The components of the stress tensor induced in the point *M(x,y,z)* are obtained by superposition:

$$\sigma_{ij}(x,y,z) = \sum_{k=0}^{Nx-1} \sum_{l=0}^{Ny-1} C_{ijkl} p_{kl} \tag{12}$$

where the influence function $C_{ijkl}(x,y,z)$ describes the stress component $\sigma_{ij}(x,y,z)$ due to a unit pressure acting in patch *(k, l)* [23].

2.2. Elastic-plastic solver

2.2.1. The solving algorithm and the computer code. A very fast algorithm has been developed to solve the pressure distribution of the wheel-rail concentrated contact.The concentrated contact loadings are characterized by very high gradients of variation of elastic or elasto-plastic components, which requires the use of a very fine meshing, the linear size of the elements being expressed in order of microns.

The Conjugate Gradient Method, with the iterative scheme proposed by [24], and a dedicated real discrete fast Fourier transform, [23, 25], have been involved in solving the system of algebraic equations.

The material was considered as having an *elastic-perfect plastic* behavior that requires for pressure to fulfill the supplementary constraint:

$$p_{ij} \geq p_Y \Rightarrow p_{ij} = p_Y \tag{13}$$

where p_Y is the value of the pressure able to initiate the plastic yield.

2.2.2. The contact geometry and rigid separation rail and wheel. The wheelset and track gauges are shown schematically in figure 5. The track gauge is measured between the points on the rail profile located inside the track at a distance of 14 mm from the common tangent to the profiles of both rails. Assuming the track is in a straight line, the mentioned tangent will be horizontal. The wheel radius is measured at the mean wheel circle, usually at 70 mm from the back of the wheel.

The two considered counterparts are a S1002 wheel profile and a UIC49rail. The wheel has a radius in rolling direction of 460 mm and the rail is inclined at 1/40. The inner gauge of the wheelset is 1360 mm and the track gauge is standard, i.e. 1435 mm. When the wheelset is in perfect alignment

with the track, the above dimensions would result in a lateral shift between the left wheel and rail of 3 mm. Of course, during train movement, the wheelset changes its relative position to the rail.

The standard UIC60 rail profile is defined by arcs of circles and it is geometrically given as a technical drawing. For keeping the same format as for the wheel, the circles are approximated by equations. Since the (not inclined) rail profile is symmetrical, only half of it will be described in four sections. The standard S1002 divides the wheel profile in eight sections in each these the profile being defined by a specific algebraic polynom.

The standard notation and main dimensions, involved in the contact geometry are as follows, (Figure 5): *WM* – the middle of the mounted axle; *TA* – the railway axis; track gauge: *TG =1435* [mm]; inside gauge: *IG* = 1360 [mm]; wheel radius: *Rw = 460* [mm]; rail inclination: *RI = 1/40*; lateral shift of the axle: Δy = -5÷3[mm]; yaw angle: 0°; roughness amplitude: 0.0 [μm]; wheel profiles: S1002, are described by polynomials; -rail profiles: UIC49, are described by polynomials.

2.2.3. The contact separation. The Brent's method, [27], has been incorporated into the computing scheme to find, for the unloaded conditions, the first contact point of the two surfaces. The final form for the separation $h(x, y)$ of contacting surfaces was found as:

$$h(x, y) = zw(y) + rw(y) - \sqrt{rw(y)^2 - zw(x)^2} - zr(y) \tag{14}$$

where: $zw(y)$ is wheel profile at the coordinate y; $rw(y)$ is the wheel radius at coordinate y; $zw(x)$ is the wheel profile at coordinate x; $zr(y)$ is the rail profile at coordinate y [26].

2.2.4. Material properties and load. Young modulus: E= $2.1 \cdot 10^5$ [MPa]; Poisson ratio: ν= 0.28; Yield limit corresponding to R7T steel, $R_{p0.2} = 580$ MPa; External normal load: 90 [kN].

2.3. Pressure and stress distributions in smooth wheel-rail contact

2.3.1. Pressure distributions in smooth wheel-rail contact. The elastic approach provided the pressure distributions depicted in figure 6 for lateral shift of the axle: Δy = -5÷3 [mm] and figure 8a for lateral shift of the axle Δy = -0 [mm] while the elastic-perfect plastic analysis gave the pressure distributions presented in figure 7 for lateral shift of the axle: Δy = -5÷3 [mm] and figure 8b for lateral shift of the axle Δy = -0 [mm].

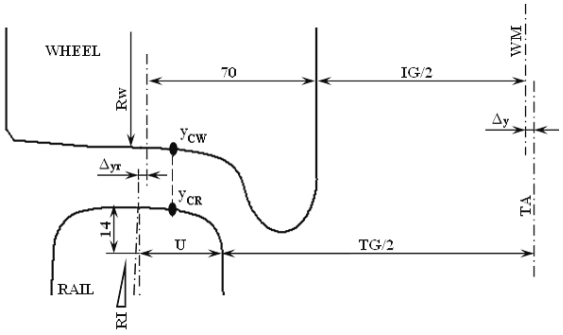

Figure 5. Wheel-rail contact geometry

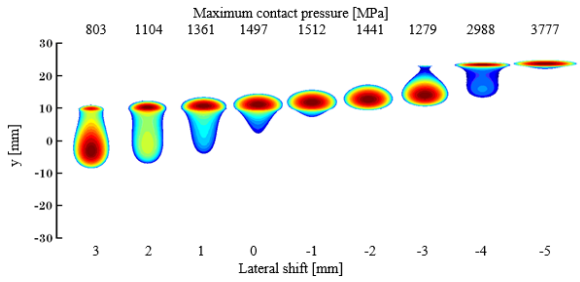

Figure 6. Wheel S1002 (polynomials)-Rail UIC49 (polynomials) elastic approach

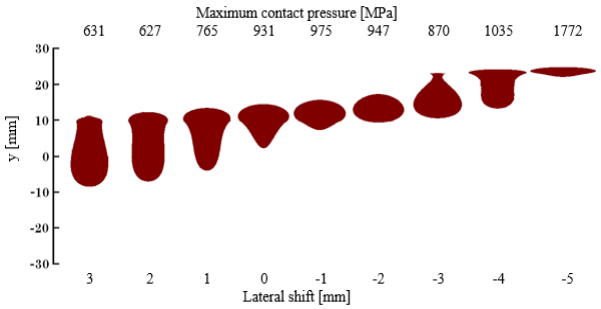

Figure 7. Wheel S1002 (polynomials)-Rail UIC49 (polynomials) elastic-perfect plastic approach

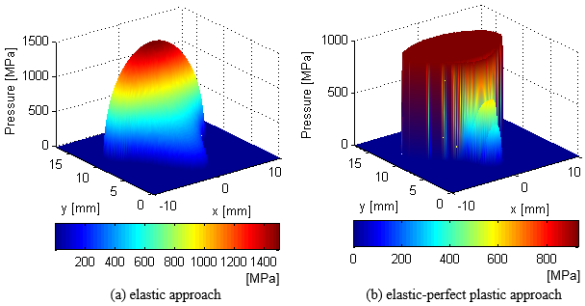

Figure 8. 3D pressure distributions for Wheel S1002 (polynomials)-Rail UIC49 (polynomials)

*2.3.2. Depth distributions of von Mises stresses.*The components of the stress tensor of any point beneath the common contact area have been obtained using the convolution expressed by equation (13). Further, the depth distributions of von Mises equivalent stress, corresponding to both, the transversal plane y-O-z and longitudinal plane x-O-z, have been carried out. Samples are exemplified in Figure 9 for the elastic approach and in Figure 10 for the elastic-perfect plastic approach.

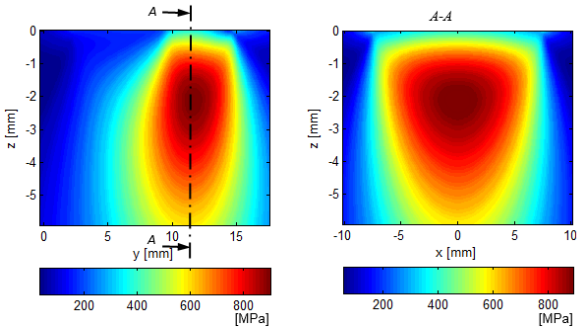

Figure 9. Von Mises Stress Distributions, elastic approach, lateral shift of the axle Δy = 0 [mm]

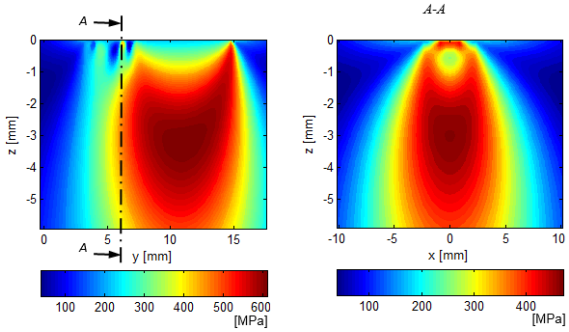

Figure 10. Von Mises Stress Distributions, elastic-perfect plastic approach, lateral shift of the axle Δy = 0 [mm]

3. Influence of roughness on pressure distribution and stress state at wheel - rail contact

The parameters used for surface microtropography characterization were as: mean height Ra, mean square deviation Rq, standard deviation σ, moment centered on the order of three Sk (Skewness), the moment centered on the fourth order K (Kurtosis), as well as the spectral parameters: mean peaks, average slope, average curvature. Measurements of roughness parameters have been performed using Form Talysurf I50 profilometer [28], and the targets were the active areas of wheel and rail surfaces for two particular running stages: new surfaces with any sign of wear, and worn surfaces, Figure 11.

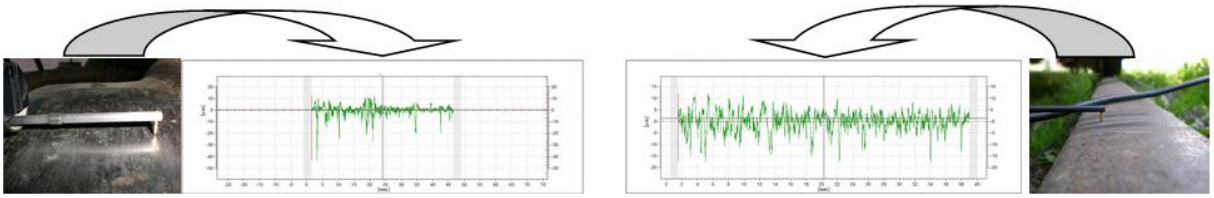

(a) Wheel (b) Rail

Figure 11. Measurements of wheel and rail roughness characterization parameters

The obtained data have been further considered in simulations and analyses to be presented in the following. The numerical simulation of surface microtopography, by imposing the desired values for the characteristic statistical parameters became a compolsory need for this stage of study. This numerical definition of roughness should include bo spatial characteristics, such as standard function.deviation σ and heights distribution $p(z)$, as well as spectral ones, in particular the autocorrelation.

The stochastic simulated roughness with mean arithmetic height Ra = 3.2 [μm] and the separation between the two bodies were overlapped. Further the pressures distributions and contact areas were evaluated for the following roughness characteristics:

- correlation parameters: $n=7$ and $m=4$, according to the elastic approach (Figure 12) and the elastic - perfectly plastic approach (Figure 14);
- correlation parameters: $n=31$ and $m=31$, according to the elastic approach (Figure 16) and the elastic - perfectly plastic model (Figure 18);
- correlation parameters: $n=63$ and $m=63$, according to the elastic approach (Figure 20) and the elastic - perfectly plastic approach (Figure 22);

The von Mises equivalent stress state was obtained for the following situations:

- correlation parameters: $n=7$ and $m=4$, according to the elastic approach (Figure 13) and the elastic - perfectly plastic approach (Figure 15);
- correlation parameters: $n=31$ and $m=31$, according to the elastic approach (Figure 17) and the elastic - perfectly plastic approach (Figure 19);
- correlation parameters: $n=63$ and $m=63$, according to the elastic approach (Figure 21) and the elastic - perfectly plastic approach (Figure 23).

The maximum pressure values obtained using stochastic simulation are shown in Table 1.

Table 1. Summary of maximum pressure values obtained using stochastic simulation

Correlation parameters	Average values	Meshing	Maximum pressure	
			Elastic approach	Elastic-perfect plastic approach
$n=7$ $m=4$	3,2 μm	256x256	2902	1017
$n=31$ $m=31$	3,2 μm	256x256	4288	1044
$n=63$ $m=63$	3,2 μm	256x256	3750	1009

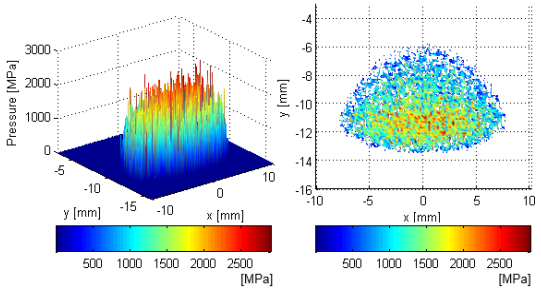

Figure 12. Pressure distributions for elastic approach *Ra = 3,2 [μm], n = 7 and m* = 4

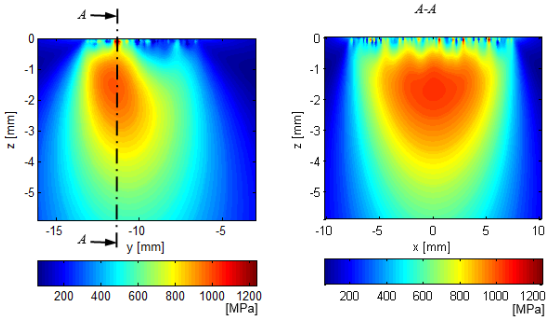

Figure 13. Von Mises Stress Distributions, elastic approach *Ra = 3,2 [μm],* $n=7$ and $m=4$

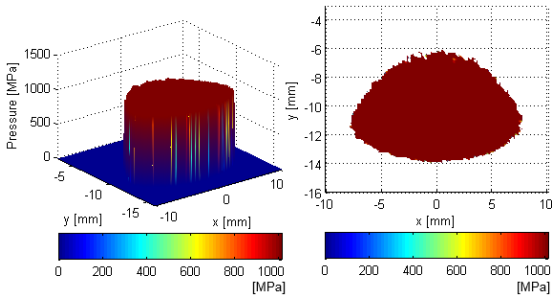

Figure 14. Pressure distributions for elastic-perfect plastic approach *Ra = 3,2 [μm],* $n = 7$ and $m = 4$

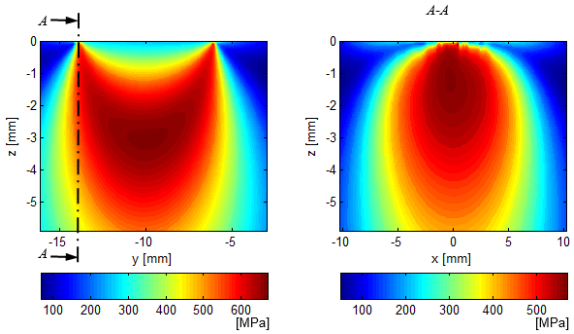

Figure 15. Von Mises Stress Distributions, elastic-perfect plastic approach, *Ra = 3,2 [μm],* $n = 7$ and $m = 4$

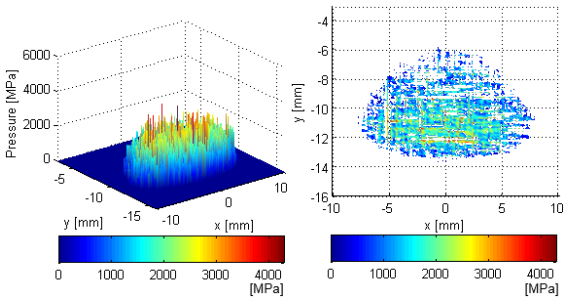

Figure 16. Pressure distributions for elastic approach *Ra = 3,2 [μm],* $n = 31$ and $m = 31$

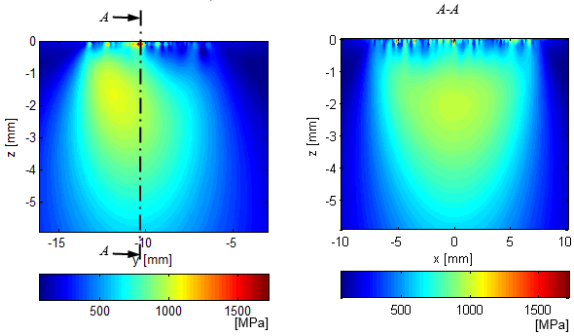

Figure 17. Von Mises Stress Distributions, elastic approach, *Ra = 3,2 [μm],* $n = 31$ and $m = 31$

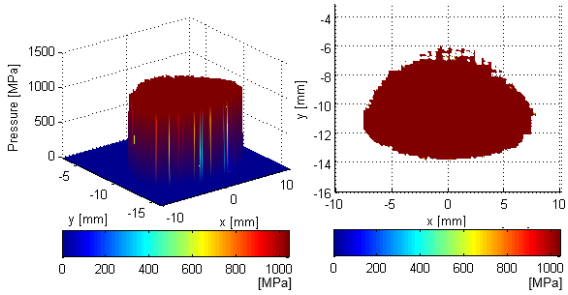

Figure 18. Pressure distributions for elastic-perfect plastic approach *Ra = 3,2 [μm],* $n = 31$ and $m = 31$

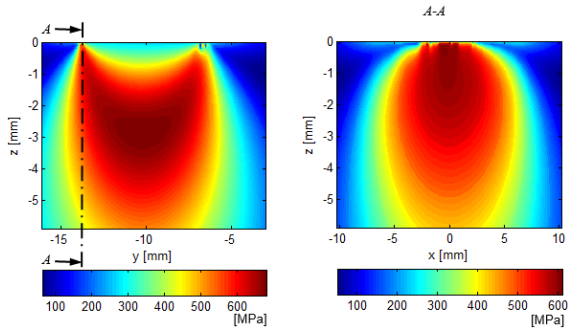

Figure 19. Von Mises Stress Distributions, elastic-perfect plastic approach, *Ra = 3,2 [μm],* $n = 31$ and $m = 31$

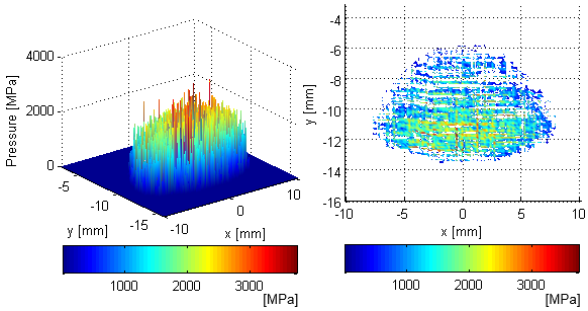

Figure 20. Pressure distributions for elastic approach *Ra = 3,2 [μm],* $n = 63$ and $m = 63$

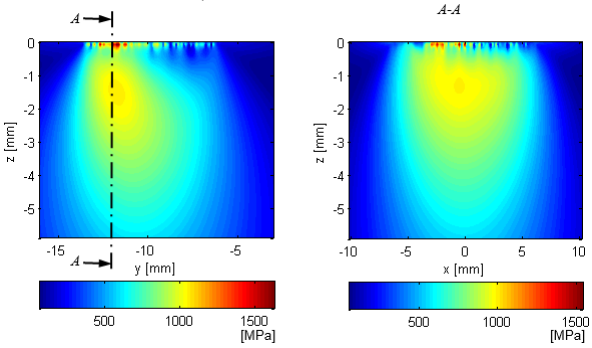

Figure 21. Von Mises Stress Distributions, elastic approach *Ra = 3,2 [μm],*

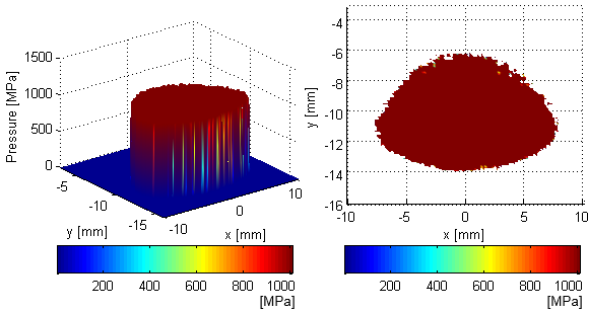

Figure 22. Pressure distributions for elastic-perfect plastic approach, *Ra = 3,2 [μm],* $n = 63$ and $m = 63$

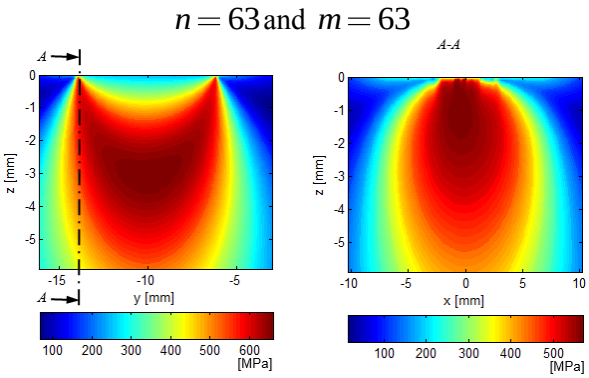

Figure 23. Von Mises Stress Distributions, elastic-perfect plastic approach, *Ra = 3,2 [μm],* $n = 63$ and $m = 63$

Although the effect of asperites appears to occur only in the immediate vicinity of the contact surface, the size and distribution of the stresses developed is considerably different from smooth contact. These differences affect the evolution of various forms of wear, which apparently would develop from the surface. The importance of subsurface tensions is reflected in the analysis of the likelihood of deterioration through contact fatigue. In this situation only a small increase in the von Mises level is able to cause a severe reduction of reliability.

4. Influence of wear on pressure distribution and stress state at wheel - rail contact

4.1 The profile measuring

During the operation, the profile of the wheel and of the railway track undergo changes caused by the evolution of various forms of wear, but especially of abrasion and contact fatigue. In order to minimize the maintenance costs of the wheel profiles and rail rails it is necessary to know the contact area and the pressure distribution achieved by the wheel-rail concentrated contacts having the geometry modified by the wear processes.

The measurements performed with MiniProf [29] instrument revieled that adue to wear processes, the profiles of the two bodies in contact suffered changes (figure 24). Another finding was that the rail gauge increases when the inside face of the rail wears at a distance bigger than 14 millimeters above the track. If for A and B cases (figure 24) the gauge track is 1435 mm, in the C and D cases it undergoes changes, being of 1437.2 mm and 1437.7 mm respectively.

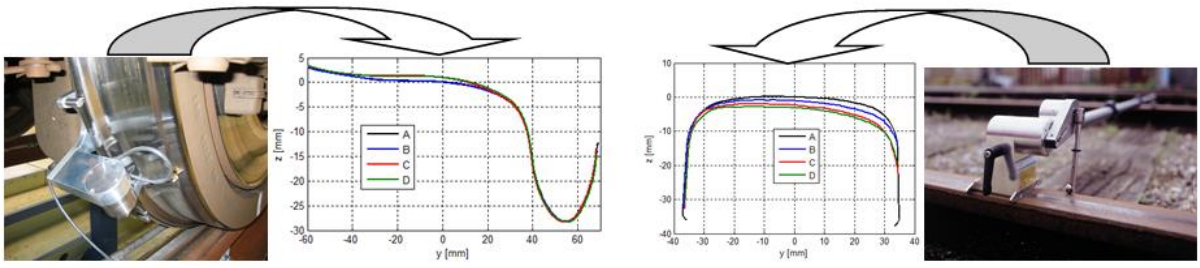

(a) Wheel (b) Rail

Figure 24. Wheel and rail profile resulted from the measurements made with Miniprof instrument: A - Profile unused, B, C, D - profiles corresponding to different stages of wear

The S1002 and S49 rail profiles for a 1/40 rail inclination and four different wheel profiles, as: the case A for unused profile and the cases B, C, D presented in figure 24 for three different stages of wear on the same wheel and rail, have been considered in the computerzed analyse. The positioning of the contact, contact area and pressure distribution for the four interaction situations have been provided by the elastic model, figures 25-28. l For the situation where the two profiles are those resulting from the manufacturing processes, Case A, the corresponding contact position, contact area and pressures distribution are presented in figure 29, For the worn profiles, Case D, the similar presentations are depicted in figure 30.

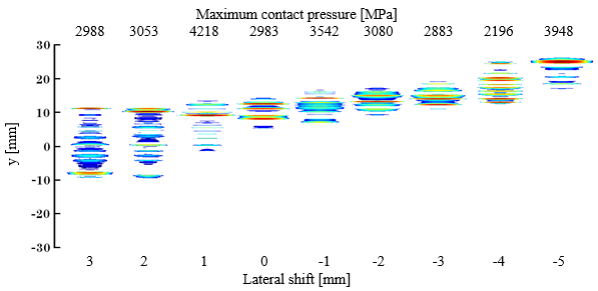

Figure 25. Pressure distributions for elastic approach, unused profiles - case A

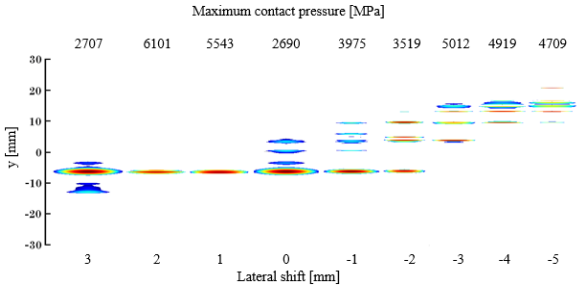

Figure 26. Pressure distributions for elastic approach, worn profiles - case B

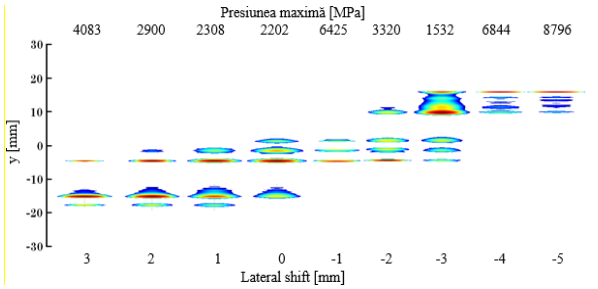

Figure 27. Pressure distributions for elastic approach, worn profiles - case C

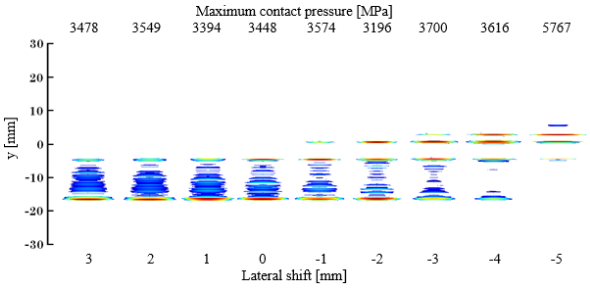

Figure 28. Pressure distributions for elastic approach, worn profiles - case D

The von Mises equivalent stress state was determined for the interaction between a S1002 and a S49 rail with a 1/40 rail inclination obtained from the Miniprof instrument measurements, for the D interaction case, lateral displacement of the wheelset 0 [mm], according to the elastic approach, resulting figure 31 and according to the elastic-perfect plastic approach, resulting figure 32 .

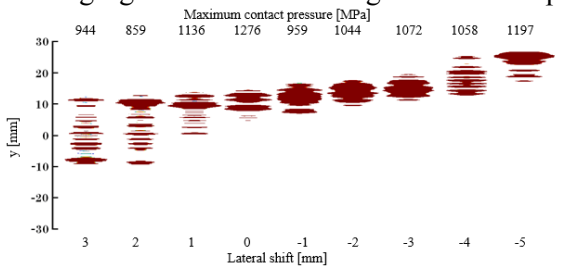

Figure 29. Pressure distributions for elastic-perfect plastic approach, unused profiles - case A

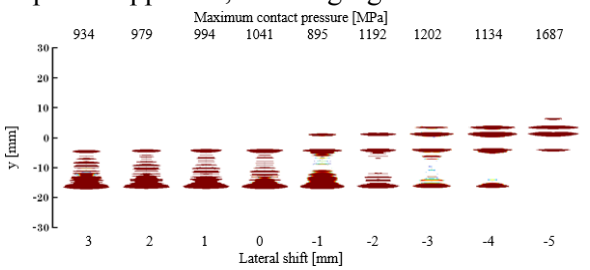

Figure 30. Pressure distributions for elastic-perfect plastic approach, worn profiles - case D

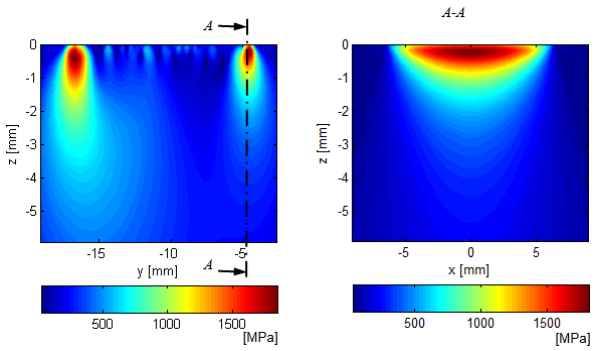

Figure 31. Von Mises Stress Distributions, elastic approach, worn profiles - case D

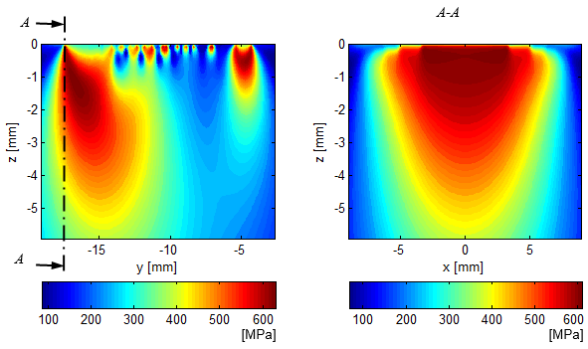

Figure 32. Von Mises Stress Distributions, elastic-perfect plastic approach, worn profiles - case D

5. Conclusions

a) A numerical solver has been involved to obtain the 3D pressure distribution in non-Hertzian wheel-rail contacts. This solver appears as a robust and fast alternative solution to the finite element models that require large memory and time resources, as well as to the experimental tests which require expensive equipments and very long duration. Using an elastic-perfect plastic body modeling, a very fast algorithm for numerical solving of the pressure distribution and stress state at the wheel-rail concentrated contact.

b) During the rolling movement, the wheel's position relative to the rail is permanently changed that affects the contact location, contact area, pressures distribution and maximum values for pressures and von Mises stresses.

c) The roughness of wheel and rail have been measured at working times corresponding to successive stages of the running in process. The measured roughness parameters have been further used to generate stochastic roughnesses with imposed heights and spatial parameters.

d) The rail and wheel surfaces with numerically generated roughness have been incorporated into an elastic-perfect plastic contact model. Even the nominal contact pressure was not able to cause von Mises stresses greater than the yielding limit, the presence of surface roughness brought on very large local asperity pressures. These discrste small areas but with high pressures induced inside the shallow layer of stressed volume von Mises stresses larger than the yield limit and accordingly possibly severe plastic deformations.

e) Wheel and rail profiles measurements have been achieved considering various stages in the wear evolution. The evolution of wear with running time caused changes regarding: the contact location and area, as well as, the pressures and von Misses stresses distributions together with their maximum values.

f) Regarding the position of the contact area, it has been noted that the more severe profiles wear was, the less influence of the wheel-set lateral shift appeared.

6. References

[1] Ayasse J B and Chollet H 2006, Wheel-rail contact *Handbook of Railway Vehicle Dynamics* S. Iwnicki (Ed.) Taylor & Francis pp 85–120

[2] Enblom R and Berg M 2008 Impact of non-elliptic contact modelling in wheel wear simulation *Wear* **265** pp1532–1541

[3] Wiest M, Kassa E, Nielsen J C O and Ossberger H 2008 Assessment of methods for calculating contact pressure in wheel-rail/switch contact *Wear* **265** pp 1439-1445

[4] Damme S 2006 *Zur Finite-Element-Modellierung des stationären Rollkontakts von Rad und Schiene* (Heft: Doctoral thesis)

[5] Knothe K, Wille R and Zastrau B 2001 Advanced contact mechanics-road and rail *Vehicle System Dynamics* **35** (4-5) pp 361-407

[6] Creţu S, Antalucă E and Creţu O 2003 The study of non-hertzian concentrated contacts by a GC-DFFT technique *Annals of University of Galati* **24** (Tribology) pp 39-47
[7] Creţu S 2009 *Elastic-Plastic Concentrated Contact* (Iaşi: Polytehnium)
[8] Ai X and Sawamiphakdi K 1999 Solving Elastic Contact Between Rough Surfaces as an Unconstrained Strain Energy Minimization by Using CGM and FFT Technique *ASME Journal of Tribology* **121** pp 639-647
[9] Allwood J 2005 Survey and Performance Assessment of Solution Methods for Elastic Rough Contact Problems *ASME - Journal of Tribology* **127** pp 10-23
[10] Bhushan B and Shaobiao C 2005 A numerical three dimensional contact model for rough multilayered elastic/plastic solid surfaces *WEAR* **259** pp 1408-1423
[11] Bhushan B, Kim T W and Cho Y J 2006 The contact behavior of elastic/plastic non-Gaussian rough surfaces *Tribology Letters* Vol. 22 No.1 pp 1-13
[12] Cai S and Bhushan B 2006 Three-Dimensional Dry-Wet Contact Analysis of Multilayered Elastic-Plastic Solids With Rough Surfaces *ASME - Journal of Tribology* Vol. 128 pp 18-31
[13] Hariri A, Zu J W, Mrad R B 2006 Modeling of Elastic-Plastic Contact Between Nominally Flat Rough Surfaces Using an n-Point Asperity Model *ASME - Journal of Tribology* Vol.128 pp 876-885
[14] Hooke C J, Li K Y and Morales-Espejel G E 2007 Rapid calculation of the pressures and clearances in rough, rolling–sliding elastohydrodynamically lubricated contacts. Part 1: low-amplitude, sinusoidal roughness *Proc. IMechE, Part C: J. Mechanical Engineering Science* **221** pp535–550
[15] Nelias D, Boucly V and Brunet M 2000 Elastic-Plastic Contact Between Rough Surfaces:Proposal for a Wear or Running-in Model *ASME - Journal of Tribology* **128** pp 236-244
[16] Urzică A and Creţu S 2010 Simulation of the non-gaussian roughness with specified values for the high order moments *The 11th International Conference of Tribology, Proceedings of ROTRIB'10*
[17] Urzică A 2011 *Research on the influence of microtopography on the state of tension developed in concentrated contacts* (Iasi: PhD thesis)
[18] Bucher F, Knothe K and Theiler A 2000 Normal and tangential contact problem of surfaces with measured roughness *5th International Conference Contact Mechanics and Wear of Rail/Wheel Systems* Tokyo Japan
[19] Bucher F 2002 *The Contact Between Micro-Rough Rails and Wheels* (Berlin: Doctoral thesis)
[20] Telliskivi T and Olofsson U 2004 Wheel–rail wear simulation *Wear* **257** pp 1145–1153
[21] Tournay H M 2008 A future challenge to wheel/rail interaction analysis and design: Predicting worn shapes and resulting damage modes *Wear* **265** pp. 1259–1265
[22] Braghin F, Bruni S and Resta F 2003 Wear of railway wheel profiles: a comparison between experimental results and a mathematical model *Vehicle System Dynamic* **37** pp 478–489
[23] Creţu S 2005 Pressure distribution in concentrated rough contacts *Buletinul Institutului Politechnic din Iasi* **LI (LV)** 1-2 pp 1-31
[24] Polonsky I A and Keer L M 1999 A numerical method for solving contact problems based on the multilevel multisumation and conjugate gradient techniques *WEAR* **231** pp 206-219
[25] Nelias D, Antalucă E, Boucly V and Creţu S 2007 A 3D semi-analytical model for elastic-plastic sliding contacts *ASME - Journal of Tribology* **129** pp 671-771
[26] Bărbîntă C I 2014 *Influence of roughness and wear on pressure distribution and stress state at wheel - rail contact* (Iasi: PhD thesis)
[27] Press W, Teukolsky S, Vetterling W and Flannery B 1992 *Numerical Recipes in C: The Art of Scientific Computing* Cambridge University Press ISBN 0-521-43108-5
[28] *** Taylor Hobson Precision *Form Talysurf Series 2 & Form Talysurf Intra Manual*
[29] *** www.greenwood.dk